JOURNAL OF GEOPHYSICAL RESEARCH, VOL. 105, NO. A12, PAGES 27,353–27,367, DECEMBER 1, 2000

On the beam speed and wavenumber of intense electron plasma waves near the foreshock edge

S. D. Bale, D. E. Larson, and R. P. Lin

Space Sciences Laboratory, University of California, Berkeley

P. J. Kellogg, K. Goetz, and S. J. Monson

School of Physics and Astronomy, University of Minnesota, Minneapolis

Abstract. Using high time resolution particle and wave data from the Wind spacecraft, we examine several crossings of the electron foreshock-solar wind boundary. We show that the most intense electron plasma waves, observed near the foreshock boundary, often occur coincident with a flux of electrons with energies between 1 keV and 27 keV. This corresponds to electron beam speeds of $9v_{th} \leq v_b \leq 50v_{th}$, rather than $v_b \approx 5v_{th}$, as is inferred from reduced distribution functions obtained by other instruments. Assuming Landau coupling, the resonant index of refraction is then $3 \leq N_0 \leq 15$, which implies that the waves are susceptible to strong scattering by ambient density fluctuations. The most intense electric fields are not well correlated with beam speed, and the distribution of electric field occurrence is broadly aligned with the interplanetary magnetic field direction. We compare the estimated maturity and bandwidth of the instability with those expected of the electrostatic decay instability and nonlinear Landau damping and find that our observations show a narrower bandwidth than expected. We suggest that the observations are consistent with scattering of electrostatic Langmuir waves to small wavenumber. The observed transverse polarization may be explained by the electromagnetic nature of the small-wavenumber z-mode, or as evidence of incident, reflected, and transmitted electrostatic components. The generation of electromagnetic emission at f_{pe} and $2f_{pe}$ is discussed in the context of the observations.

1. Introduction

The plasma microphysics of the growth, saturation, and nonlinear evolution of beam-driven electron plasma waves in the solar wind is considered unfinished business despite more than 20 years of work. This is due largely to the limited time resolution of the previous generation of space plasma instruments. An extensive amount of work has been done with the IMP and ISEE spacecraft, and these observations and their interpretation form most of the body of our present understanding.

In part, the generation of electron plasma waves is interesting because these waves are the energy source of freely propagating electromagnetic emission at the fundamental and harmonic of the electron plasma frequency (f_{pe} and $2f_{pe}$). The phase speed of these waves is greater than light speed, and hence they are not generated by Landau resonance with energetic electrons. The paradigm is that the f_{pe} and $2f_{pe}$ emissions are generated by the nonlinear coupling of electrostatic Langmuir waves with sound waves or other Langmuir waves, respectively. It is these emissions that allow the remote detection of solar radio bursts and planetary foreshocks, as well as the distant heliopause.

In the case of the terrestrial foreshock, electrons energized by the bow shock [e.g., *Anderson et al.*, 1979] stream back into the solar wind and form a beam-like feature near the upstream tangent field line due to time-of-flight effects [*Filbert and Kellogg*, 1979]. This beam is unstable to the generation of electrostatic Langmuir waves at the Landau resonance ($k \approx \omega_{pe}/v_b$), and the intensity of the waves falls off deeper into the foreshock [*Filbert and Kellogg*, 1979; *Etcheto and Faucheux*, 1984]. A statistical survey of Wind data [*Bale et al.*, 1997] showed that the global probability distribution of plasma waves amplitudes goes as $P(E) \approx 1/E^2$. Recently, *Cairns and Robinson* [1997, 1999] have shown that this distribution can be deconvolved by a lognormal distribution and is consistent with the stochastic growth theory of wave evolution used to describe the evolution of Langmuir waves in type III source regions [e.g., *Robinson*, 1992; *Robinson and Cairns*, 1993].

Paper number 2000JA900042.
0148-0227/00/2000JA900042$09.00

Radio emission is found to be most intense just at the foreshock edge [*Lacombe et al.*, 1988; *Reiner et al.*, 1997], and mode conversion of the intense electron plasma waves is the likely agent. Radio emission at $2f_{pe}$ is thought to result from the coalescence of two Langmuir waves (denoted $L + L' \rightarrow T$) [*Ginzburg and Zheleznyakov*, 1959; *Cairns*, 1988]. For short-wavelength waves, this requires oppositely directed Langmuir waves, and the backward going wave may be obtained from either an electrostatic decay instability ($L \rightarrow L' + S$) or by wave scattering in density fluctuations [*Yin et al.*, 1998c]. In the former case, the coalescence process is slaved to the decay instability and requires large-amplitude Langmuir waves; the latter requires the breakdown of the Wentzel-Kramers-Brillouin (WKB) approximation for Langmuir wave propagation in the solar wind. At longer wavelengths, $k_L \approx k_T/2$, coalescence to $2f_{pe}$ may occur between two nearly colinear Langmuir waves [*Willes et al.*, 1996], and indeed this process has the highest emission rate; it requires, however, that the Langmuir waves are scattered out to long wavelengths by density fluctuations [*Krauss-Varban*, 1989] and that WKB is not violated in the process.

Radio emission at f_{pe} may arise by either a nonlinear coupling of Langmuir waves with ion sound waves ($L \rightarrow S + T$ or $L + S \rightarrow T$) or linear mode conversion by tunneling of the z-mode to the o-mode branch. The former case requires the existence of ion acoustic turbulence, while the latter requires special conditions on the density fluctuation spectrum.

Recent waveform observations of plasma waves near the foreshock edge [*Bale et al.*, 1998; *Kellogg et al.*, 1999] show that they are observed as having rotating electric fields, not the purely longitudinal polarization expected of Langmuir waves. The phase shift between components is a function of angle to the interplanetary magnetic field (IMF) and it was argued that this is evidence of scattering to long-wavelength z-mode waves, as had been predicted by *Krauss-Varban* [1989]. A result in accordance with this was obtained by *Scarf et al.* [1970] by using instruments on the OGO 5 spacecraft. OGO 5 was equipped with a small electrostatically shielded magnetic loop antenna filtered to receive at 70 kHz. During the passage of a high-density region, after an apparent coronal mass ejection (CME), *Scarf et al.* [1970] measured both the electric and magnetic field intensity at 70 kHz (the local plasma frequency). They compared the electric and magnetic intensities to estimate the index of refraction and found values between $N \approx 0.1$ and 1, with occasional excursions to $N \approx 10$. They argued, from the dispersion relations, that this was evidence of z-mode wave activity.

The various theories depend strongly on the resonant wavenumber of the initial instability, and that wavenumber is related simply to the electron beam speed $k \approx \omega_{pe}/v_b$. In particular, the modulational instability has been shown to be unimportant for beam speeds of less than $v \approx 90v_{th}$ [*Cairns et al.*, 1998]. Furthermore, the dispersion relation for Langmuir/z-mode waves in the solar wind is such that the WKB motion of the waves in density gradients is strongly dependent on the initial wavenumber. Observations of positive slope features, and hence electron beams, in reduced electron distribution functions have been made with the ISEE [*Fitzenreiter et al.*, 1984] and Wind [*Fitzenreiter et al.*, 1996] spacecraft with typical beam speeds of $v_b \approx 5v_{th}$, and this beam speed is often used as input to theory.

In this paper, we use the instuments on the Wind spacecraft to study the electron foreshock edge region. The Wind spacecraft is equipped with state-of-the-art instruments to measure plasma waves [*Bougeret et al.*, 1995] and three-dimensional electron and ion distribution functions [*Lin et al.*, 1995], as well as magnetic field [*Lepping et al.*, 1995].

The structure of the paper is as follows: In section 2, we describe the instruments and data used in this study. In section 3, we analyze three foreshock edge events in some detail; here we show that the electron beam responsible for intense wave growth at the foreshock edge is typically at greater than 1 keV. We then show that the bandwidth of the observed plasma waves is very small, indeed probably limited by the instrument frequency resolution. We also reiterate the previous observation that the intense plasma waves near the foreshock edge are observed as transverse, with rotating, not longitudinal, electric field vectors. In section 4, we compile our results to conclude that the intense waves observed near the foreshock edge are probably not beam resonant Langmuir waves, but have been scattered to long wavelengths by the ambient solar wind density fluctuations. We qualitatively discuss the generation of f_{pe} and $2f_{pe}$ radio emission in the context of our conclusions, and in section 5 we summarize our results.

2. Instruments and Data

The Wind spacecraft was launched on November 1, 1994, into a series of phasing orbits that preceded several months at the L1 libration point. The spacecraft has returned for phasing and lunar swingby maneuvers several times; these orbits give very good coverage of the terrestrial electron foreshock, as well as measuring in situ interplanetary type III radio bursts. Here we present data from several Wind perigee passes in 1996 and 1997. We use high-resolution data from the WAVES [*Bougeret et al.*, 1995] and Three-Dimensional Particle (3DP) [*Lin et al.*, 1995] instruments, as well as spin resolution magnetic field data from the Magnetic Fields Investigation (MFI) instrument [*Lepping et al.*, 1995], all on the Wind spacecraft.

2.1. Particle Measurements

Electron measurements from the 3DP experiment are provided from separate instruments. Two electrostatic analyzers (EESAs) make three-dimensional measure-

ments of electron distributions from 3 eV to 30 keV. The EESA-L analyzer covers the range of 3-1000 eV with a smaller geometric factor than the EESA-H analyzer, which covers the energy range 300 eV to 30 keV. EESA-L can be put into a burst mode, returning contiguous spin resolution (3 s) three-dimensional distribution functions. The duty cycle of the EESA-H instrument is typically much lower. The Solid State Telescope (SST-F) is a semiconductor detector that counts electrons in the energy range of 27-510 keV with $\Delta E/E \approx 30\%$. A thin lexan foil shield rejects protons up to several hundred keV and is coated to eliminate sunlight. An anticoincidence circuit, with an adjacent detector, eliminates counts from penetrating particles, providing a very low background count. Solar wind velocity moments from the PESA-L ion electrostatic analyzer are used as well.

2.2. Wave Measurements

The WAVES instrument consists of several components with specific scientific targets; the instrument is described in detail by *Bougeret et al.* [1995]. We use data from the Thermal Noise Receiver (TNR) and Time Domain Sampler (TDS) components to characterize the upstream electron plasma waves.

The TDS is a "snapshot" waveform sampler with programmable sample speeds, bandwidth, and data selection algorithm. During the interval analyzed here, the TDS was configured to sample the two orthogonal spin plane antennas at 120,000 samples per second; the Nyquist frequency is therefore 60 kHz, well above the average solar wind electron plasma frequency and allowing full temporal resolution of electron plasma waves. The antennas are wire dipoles of length $L_x = 100$ m and $L_y = 15$ m tip to tip. The TDS generates 2048 point events, with the peak signal centered in the interval. These data are buffered on board and sorted by absolute amplitude; the largest events then get put into the telemetry stream preferentially. Smaller events frequently fall off the back of the buffer as larger events are sampled. In this way, the TDS can identify regions of intense wave activity quite easily.

The TNR is a very sensitive digital spectrum analyzer designed to do thermal noise spectroscopy in the ambient solar wind plasma [e.g., *Meyer-Vernet and Perche*, 1989]. The TNR consists of several separate receivers that measure and digitize into different frequency bands from 4 kHz to 256 kHz.

3. Analysis

In this section we discuss three separate foreshock encounters by Wind. In each case, Wind measures intense electron plasma waves in both the TNR and TDS instruments. The TDS selection algorithm chooses the most intense events and, hence, selects the time of intense wave observation to within milliseconds. As was discussed above, the 3DP instrument can be operated in a burst mode, returning contiguous 3-s electron distributions. This burst mode is usually triggered by proton events; however, during the April 1996 perigee pass, the burst mode was triggering randomly and captured several foreshock crossings. The third event is a slower crossing, with continuous energy coverage, albeit not in burst mode.

3.1. Case 1: April 20, 1996, 0312:00 UT

Plate 1 shows a summary plot of data from a foreshock edge encounter approximately at 03:12:00 UT on April 20, 1996. The top panel shows data from the TNR receiver. The solar wind electron plasma frequency is visible as a band at approximately 15 kHz, and the electromagnetic second harmonic (hereinafter $2f_{pe}$) at about 30 kHz. The middle panel shows the occurrence and peak amplitude of triggered TDS waveform measurements. The TDS measurements, as described above, are taken from the 100-m dipole (X) antenna and are buffered and sorted on board. Therefore the location of these waveform events represents the most intense wave activity and is seen to be concentrated just at the foreshock edge. The bottom panel shows electron energy flux, in units of eV/s/cm^2/sr/eV, from the EESA-L electrostatic analyzer (up to approximately 1 keV) and the SST-F solid state detector (above 27 keV), both in burst mode.

The EESA-L data are transformed into the local solar wind frame, after correcting for spacecraft potential effects, and then organized by pitch angle. The energy flux shown in Plate 1 is only that directed away from the bow shock, in this case with pitch angle greater than 90^o. The SST-F data are also organized by pitch angle and only the backstreaming portion is shown. Spacecraft potential effects, and solar wind frame transformations, are negligible in the energy range of the SST-F.

It is obvious from this figure that many of the intense plasma waves are found when the flux in the 1-keV channel of EESA-L is near background and the flux in the SST-F detector is high. Figure 1 shows the energy flux of the two detectors as a function of energy at 0313:34 UT. At this time, four TDS waveform events are observed with an average amplitude of 65 mV/m and maximum of 102 mV/m. In the top panel of Figure 1, the circles show the energy flux, while diamonds show the solar wind background. The EESA-L analyzer measures electrons to 1 keV, and the SST-F, above 27 keV. The bottom panel of Figure 1 shows the energy flux minus the background. Only flux above background is shown, and the solid line represents 3 standard deviations above the background. The bottom panel shows that only $E > 27$ keV, and less than 80 keV, electrons are measured coincident with these waves, though obviously the flux extends to lower energies. Since the electron thermal speed is approximately 2200 km/s for this event, this implies that the electron beam responsible for these waves lies in the range $8.5 < v_b/v_{th} < 44$.

Figure 2 shows the same quantities for the time 0314:43 UT, deeper in the electron foreshock. One TDS

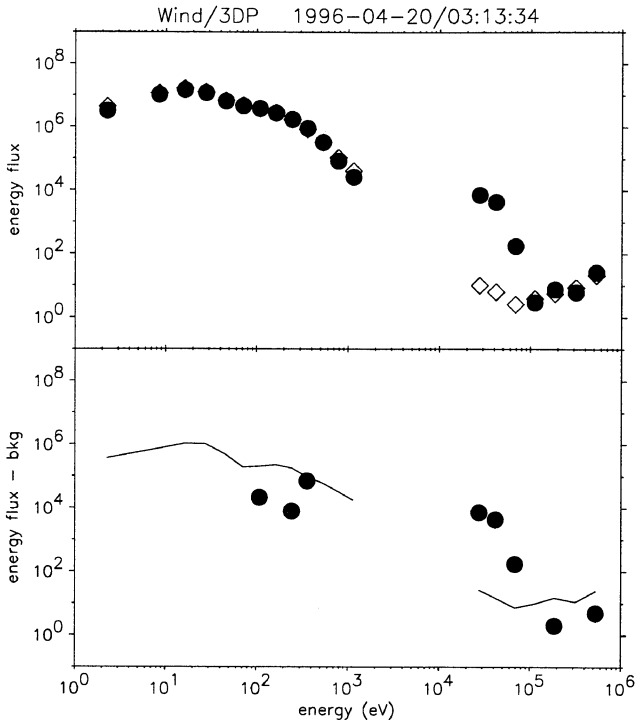

Figure 1. Electron energy spectrum from the EESA-L and SST-F detectors, showing electron energy flux directed away from the bow shock during an interval of intense TDS wave activity at 0313:34 UT on April 20, 1996 (see Plate 1). (top) Electron flux during the waveform event (circles) and a background in the solar wind (diamonds). (bottom) Background plus 3σ as a solid line, with positive values of flux minus background as circles. Only above 27 keV and up to about 80 keV is there significant electron flux during the intense wave events.

waveform event is measured here with a peak amplitude of 54 mV/m. This spectrum shows the beam extending down to lower energies, approximately 300 eV or $v_b \approx 4.7\ v_{th}$; this is similar to previously reported observations [e.g., *Fitzenreiter et al.*, 1984; 1996]. Electron spectra during intense wave activity for two other edge crossings at 0314:28 UT and 0315:15 UT are similar to the data in Figure 1 in that they show no significant flux below 1 keV.

During this interval, the average solar wind speed was $v_{sw} \approx 663$ km/s, proton temperature $T_p \approx 31$ eV, electron temperature $T_e \approx 14$ eV, average density $N_p \approx 2.6$ cm^{-3} and the magnetic field strength was $|B| \approx 5.8$ nT. The spacecraft was approximately 34 R_E away from Earth, in the electron foreshock.

3.2. Case 2: April 21, 1996, 0655:00 UT

Plate 2 is a summary plot of the foreshock edge on April 21, 1996 at 0655 UT; the data and format are the same as Plate 1. This event was also recently described by *Yin et al.* [1998a], who compared EESA-L distribution functions and wave spectra from the TNR instrument with the results of a particle-in-cell (PIC) simulation.

Intense wave activity, shown by the location of the TDS events, is concentrated just at the foreshock boundary; rising or falling flux in the 1-keV channel of EESA-L accompanies the events in this time interval. Figure 3 shows that only >27-keV electron flux is statistically significant during the first burst of waves at 0655:30 UT. The burst at 0658:18 UT, with three TDS events and peak amplitude of 79 mV/m, shows strong flux above ≈300 eV in EESA-L (Figure 4), though the spacecraft is clearly exiting the foreshock and time aliasing might be a concern.

During this interval, the average solar wind speed was $v_{sw} \approx 572$ km/s, proton temperature $T_p \approx 25$ eV, electron temperature $T_e \approx 12$ eV, average density $N_p \approx 2.8$ cm^{-3}, and the magnetic field strength was $|B| \approx 6$ nT. The spacecraft was approximately 49 R_E away from Earth, in the upstream solar wind.

3.3. Case 3: June 13, 1997, 0230:00 UT

Our last example (Plate 3) is a slower crossing of the foreshock boundary where we can resolve the boundary without burst mode particle data. Plate 3 is identical to the above summary plots, except that it includes data from the EESA-H analyzer in the energy range 130-27,000 eV. The EESA-H analyzer has a very large geometric factor and suffers, at large energy, from a large background count; the background is due to scattered solar wind protons and photons. In Plate 4, we show

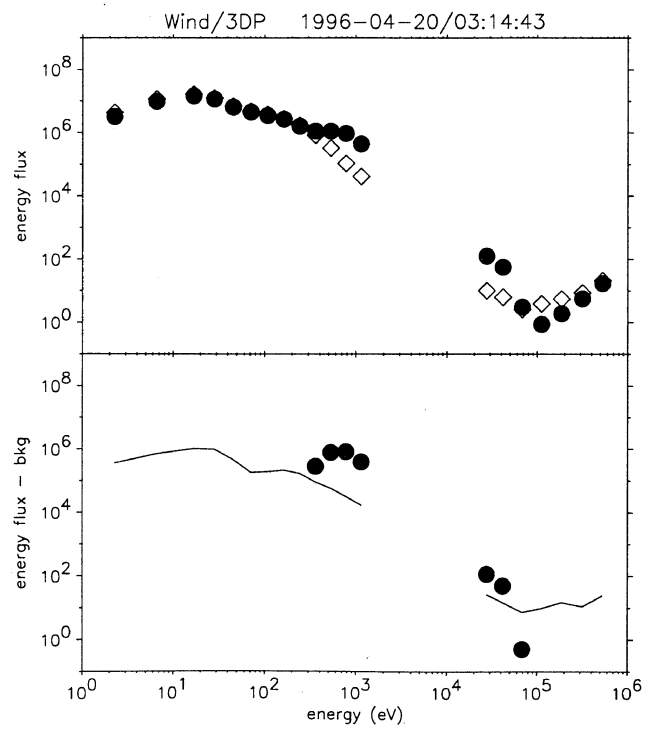

Figure 2. Electron energy flux during another TDS waveform event on April 20, 1996, in the same format as Figure 1. This event shows statistically significant flux down to a few hundred eV and is accompanied by less intense plasma waves.

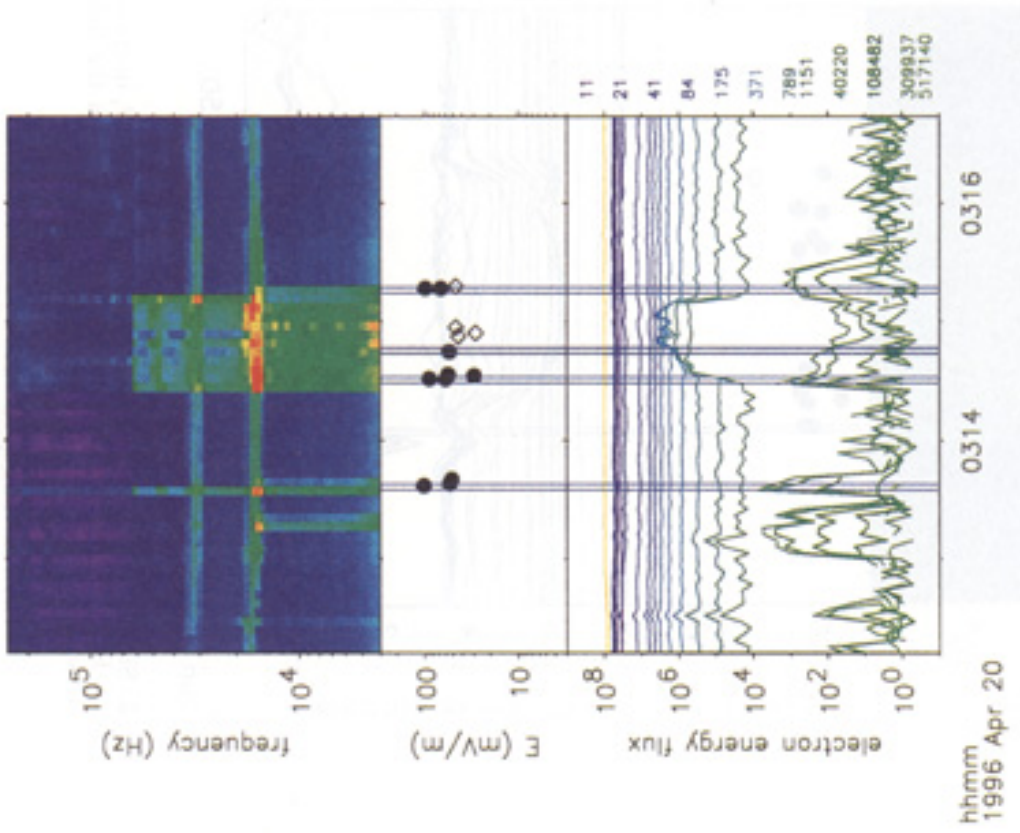

Plate 1. Electron foreshock edge encounter on April 20, 1996. (top) Data from the TNR receiver, showing the electron plasma line at approximately 15 kHz. The strong enhancements at f_{pe} are beam-driven electron plasma waves. (middle) Occurrence and amplitude of TDS waveform events. Circles are events selected for large amplitude, while diamonds are randomly selected events. (bottom) Burst data from the EESA-L and SST-F detectors and shows electron energy flux directed away from the bow shock in the range from 8 to 1100 eV (EESA-L) and 27 to 511 keV (SST-F). The most intense electron plasma waves occur when the flux in the EESA-L detector is near background, while the SST-F shows flux above 27 keV.

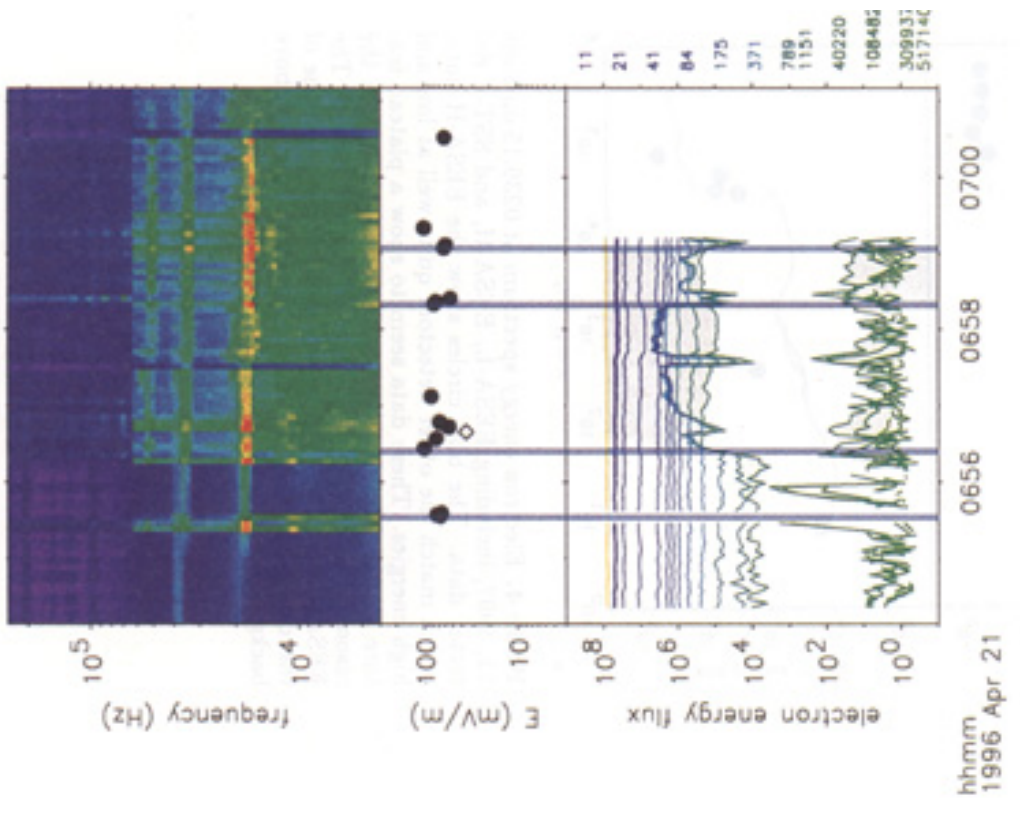

Plate 2. Electron foreshock encounter on April 21, 1996, in the same format as Plate 1. Again, the most intense wave activity occurs where electron flux at 1 keV is at background, or just beginning to rise.

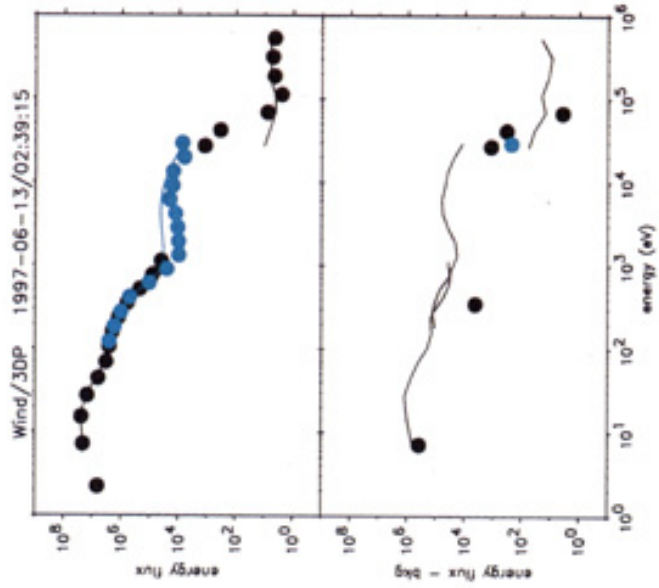

Plate 4. Electron energy spectrum at 0239:15 on June 13, 1997, including EESA-L, EESA-H, and SST-F detector data. The blue circles show the EESA-H data, which match the other detectors quite well at low and high energies. These data seem to show a plateau feature at around a few keV, and this could well be the resonant energy for the electron plasma waves. The EESA-H detector is, however, quite noisy, and none of the data below about 25 keV are significantly above background.

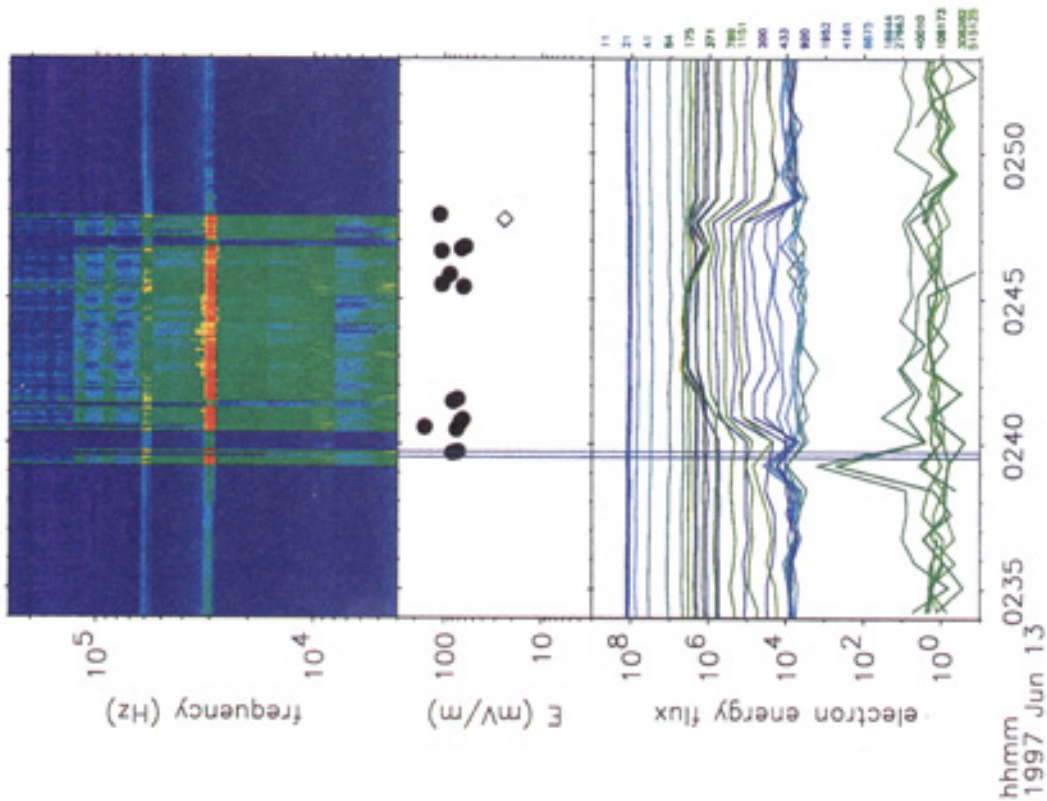

Plate 3. Slower foreshock edge crossing on June 13, 1997, in the same format as Plate 1. This event includes EESA-H data in the bottom panel and so covers the entire energy range.

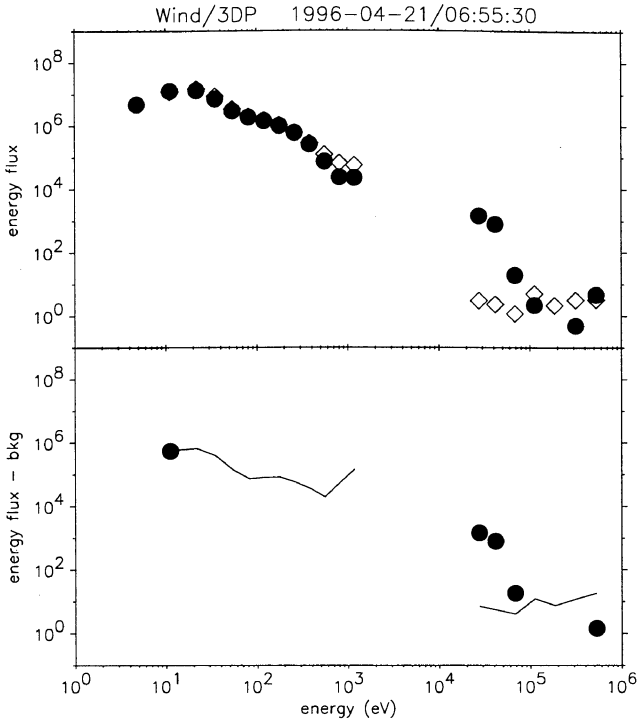

Figure 3. Electron energy flux in EESA-L and SST-F at 0655:30 UT on April 21, 1996. Again, significant flux occurs only in the SST-F detector, at energies greater than 27 keV and up to about 80 keV.

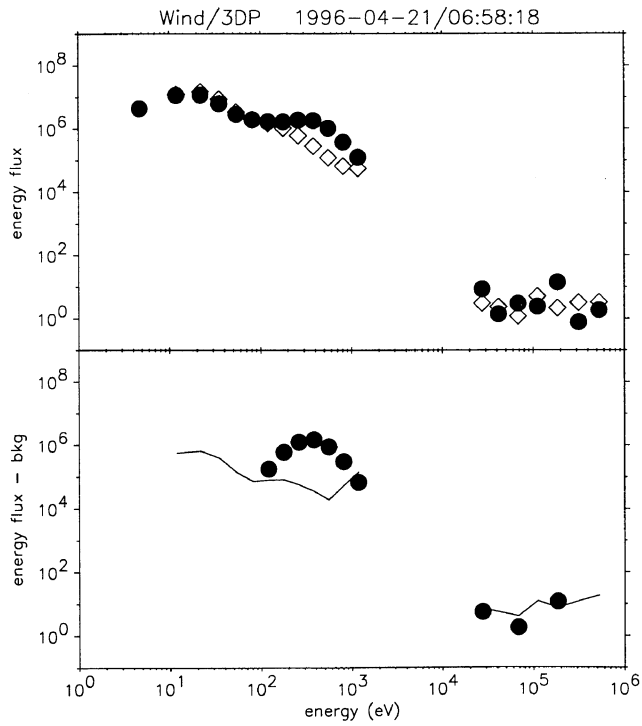

Figure 4. Event similar to Figure 2, on April 21, 1996, showing only significant electron flux at lower energies. This type of event is consistent with other reduced distribution function measurements of foreshock beams [e.g., *Fitzenreiter et al.*, 1996].

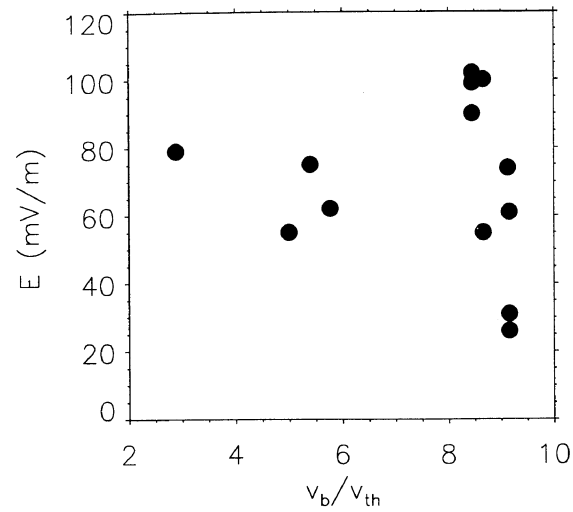

Figure 5. Peak wave amplitude against electron beam speed, in units of measured electron thermal speed. All events above $v_b/v_{th} \approx 8$ correspond to electron flux above 1 keV (out of the range of EESA-L). There is alot of variation in amplitude for these most energetic events, but no clear trend.

the full energy spectrum during the foreshock crossing at 0239:15 UT. This plot is like the others above, except that it now includes data from the EESA-H analyzer, as blue circles. The EESA-H data overlap nicely with EESA-L on the low-energy end (≈130-1000 eV) and seem to meet the SST-F detector levels at the high-energy end (27 keV). However, as was noted above, the level of background is quite high in the detector, and none of the EESA-H data are above the 3σ statistical uncertainty level. The data seem to show a plateau between 1 and 5 keV or so, which could correspond to the energy of resonant electrons; however, the noise background precludes making that statement conclusively.

During this interval, the average solar wind speed was $v_{sw} \approx 350$ km/s, proton temperature $T_p \approx 5.3$ eV, electron temperature $T_e \approx 12$ eV, average density $N_p \approx 9.6$ cm^{-3}, and the magnetic field strength was $|B| \approx 3.8$ nT. The spacecraft was approximately 29 R_E away from Earth, in the upstream solar wind.

3.4. Peak Electric Field and Electron Beam Speed

In Figure 5, we show the peak electric field, within an electron measurement interval, plotted against the normalized electron "beam" speed v_b/v_{th}. These are data from 13 foreshock edge encounters, on April 20, April 21, and October 20, 1996, with burst mode data. All of the events with $v_b/v_{th} \geq 8$ correspond to events that appear in the SST-F detector but not the EESA-L. This implies that the wave resonant electrons have energies greater than 1 keV; the variation in v_b/v_{th} is due to variations in the electron thermal speed. All of these high-speed events show enhanced flux in the

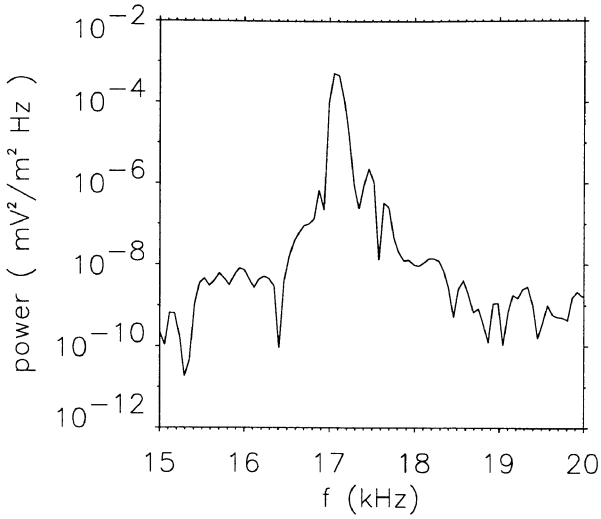

Figure 6. Power spectrum of an intense electron plasma wave event as measured by the TDS instrument. The FWHM bandwidth of the events is $\Delta f/f \approx 0.0034$.

lowest-energy channel of the SST-F, which means that the beam speed is less than 27 keV, or $v_b/v_{th} \leq 47$.

There is no clear trend in Figure 5, although the very largest events occur for beam speeds greater than $8v_{th}$. The average amplitude of these waves is 70 mV/m, which gives an average dimensionless energy $\bar{W} = \epsilon_0 E^2/4nkT_e \approx 2.2 \times 10^{-3}$, using typical plasma density and temperature, although several TDS events with peak values greater than 100 mV/m are observed. So while it is generally true that the largest-amplitude waves are found nearest the foreshock edge [*Filbert and Kellogg*, 1979; *Etcheto and Faucheux*, 1984], we do not find a strong trend when comparing the most intense waves ($E > 20$ mV/m) with the beam speed, although our resolution of the beam speed above 1 keV is limited.

3.5. Amplitude and Bandwidth of Electron Plasma Waves

Langmuir waves grow out of the electrostatic thermal noise background when a source of energy is present. In the ambient solar wind, thermal noise exists at a typical level of $E_{th} \approx 7 \times 10^{-4}$ mV/m around the electron plasma frequency. For Langmuir waves to grow to 70 mV/m requires $\gamma t \approx 11.5$ e foldings of growth. Then $\omega_{pe} t \approx 11.5/(\gamma/\omega_{pe})$, which can be compared with theoretical growth rates to estimate the maturity of the instability.

The growth rate of Langmuir waves near the foreshock edge has been calculated by many authors [e.g., *Filbert and Kellogg*, 1979; *Cairns*, 1987; *Yin et al.*, 1998a] Recently, *Yin et al.* [1998a] calculated the linear growth rate of electrostatic Langmuir waves by using a model time-of-flight electron beam as an energy source. In their model, a time-of-flight velocity cutoff was superposed on a Lorentzian electron distribution to model the electron flux near the foreshock edge. They then calculated the growth rate of Langmuir and beam modes for various cutoff beam speeds. For a beam speed of $v_b/v_{th} \approx 9$, which is the largest they consider, they find a maximum growth rate of $\gamma/\omega_{pe} \approx 0.009$, at the Landau resonance $k \approx \omega_{pe}/v_b$. Although our inferred beam speed (>1 keV) would imply a smaller growth rate, we use the result of *Yin et al.* [1998a] as a conservative estimate. With $\gamma/\omega_{pe} \approx 0.009$ and 11.5 e

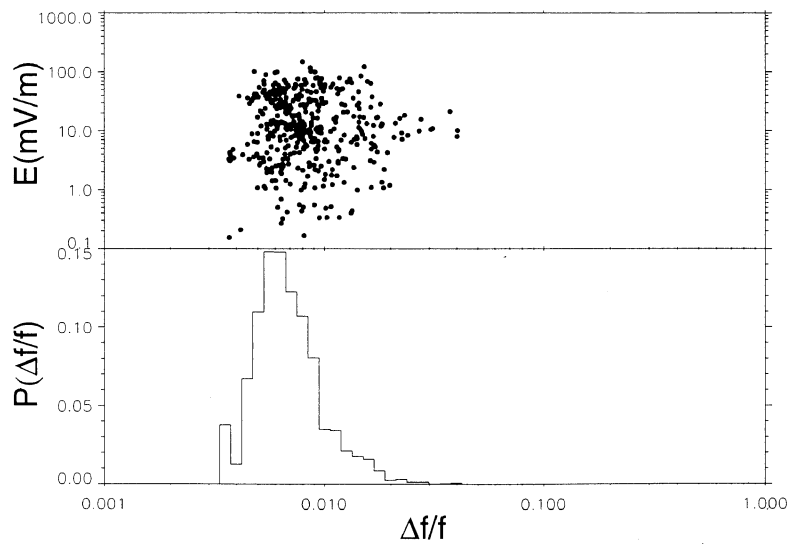

Figure 7. Bandwidth statistics for several hundred intense waveform events. The bandwidth is full width/half maximum (FWHM) from the power spectrum interpolated around the peak frequency. (top) Peak wave amplitude against bandwidth $\Delta f/f$. There is no obvious trend. (bottom) Histogram of bandwidths. The peak of this probability distribution occurs at $\Delta f/f \approx 0.006$.

foldings of growth, the instability can be estimated to be $\omega_{pe}t \approx 11.5/(\gamma/\omega_{pe}) \approx 1278$ cycles old.

Figure 6 shows the power spectrum of a TDS waveform event near the foreshock edge on April 21, 1996. The power spectrum is calculated with a Hanning window. The peak amplitude of this event is 75 mV/m, and the bandwidth, as can be seen, is very small; the peak power is approximately 5.2×10^{-4} mV^2/m^2 Hz. The full width at half maximum (FWHM) bandwidth of this wave is limited by the frequency resolution of the instrument, $\Delta f \approx 58$ Hz, which gives $\Delta f/f \approx 0.0034$.

Figure 7 shows the calculated bandwidth for 537 intense wave events near the foreshock edge; these events are chosen to have the peak frequency in the range $(0.9f_{pe}, 1.3f_{pe})$, where f_{pe} is calculated by using the local proton density. In the top panel of Figure 7, the wave amplitude is plotted against bandwidth $\Delta f/f$. The FWHM bandwidth is calculated by interpolating around the peak to plus and minus the half maximum power. The bottom panel is the probability distribution of bandwidth $P(\Delta f/f)$ of all 537 events. The peak in the probability distribution lies at $\Delta f/f \approx 0.006$. Again, this number may be limited by the frequency resolution of the instrument and the large variation in values results from the variation in f_{pe}. This observed narrow bandwidth is generally true of the most intense waves near the foreshock edge and has been shown previously using TDS data [*Bale et al.*, 1997] and with other spectral density measurements [e.g., *Etcheto and Faucheux*, 1984; *Yin et al.*, 1998a]. It should be noted that spectral density instruments typically have much poorer frequency resolution than a waveform measurement. For example, the TNR instrument on Wind has frequency resolution $\Delta f/f \approx 1/23 \approx 0.044$ so that the best resolution is approximately 1 kHz for typical solar wind electron densities. The most intense waves in the foreshock and interplanetary type III bursts, however, generally have much smaller bandwidths than this.

In the simulations of *Yin et al.* [1998b], the electrostatic waves did not succumb to either parametric decay instability or modulational instability, consistent with the results of *Cairns et al.* [1998]. The instability plateaued the unstable electron distribution function quasi-linearly, and nonlinear Landau damping broadened the k space spectrum of the waves. In the work of *Yin et al.* [1998b], the spectrum was broadened to about $\Delta k/k \approx 0.5$ after approximately $\omega_{pe}t \approx 550$ plasma periods. This corresponds to a Doppler-shifted frequency spread of $\Delta f/f = (\Delta k/k)\,(v_{sw}/v_b) \approx 0.0125$ (assuming a beam speed $v_b \approx 10\ v_{th}$); this is a factor of 2 more than the peak in our observed bandwidth distribution.

The electrostatic decay instability would also broaden the power spectrum. As a backward propagating Langmuir wave grows at a wave vector $\vec{k}_{L'} \approx -\vec{k}_L$, it would appear at a Doppler-shifted frequency of $\omega \approx \omega_{pe} + \vec{k}_{L'} \cdot \vec{v}_{sw}$. Since the initial and daughter waves have approximately oppositely directed wave vectors, the Doppler splitting should be $\Delta\omega \approx 2k_L\ v_{sw}\ \cos\theta_{vB}$, where θ_{vB} is the angle between the IMF and solar wind directions (assuming a field-aligned beam, and hence field-aligned initial wave vector). Since $k_L \approx \omega_{pe}/v_b$, this gives splitting $\Delta\omega/\omega_{pe} \approx 2v_{sw}/v_b\ \cos\theta_{vB} \approx 0.05\ \cos\theta_{vB}$ for typical parameters. Although we do occasionally observe splitting and structure in the power spectrum [e.g., *Kellogg et al.*, 1996], the largest events observed by the TDS tend to be very monochromatic [*Bale et al.*, 1997]. Growth rates of the electrostatic decay instability are, however, typically quite low. *Goldman et al.* [1996] find evidence of backscattered Langmuir waves only after several thousand plasma periods, in a one-dimensional Vlasov simulation.

3.6. Polarization of Electron Plasma Waves

In previous papers [*Bale et al.*, 1998; *Kellogg et al.*, 1999], we showed that the observed polarization of the electron plasma waves in the foreshock is not strictly longitudinal but is a function of the angle to the IMF. Figure 8 is an example of the plasma wave polarization of a TDS event during the interval of Plate 1 (April 20, 1996, 0313:37 UT). The top two panels correspond to the measured X and Y electric fields; the third panel shows the phase between X and Y, and the bottom panel consists of hodograms of the two components. It

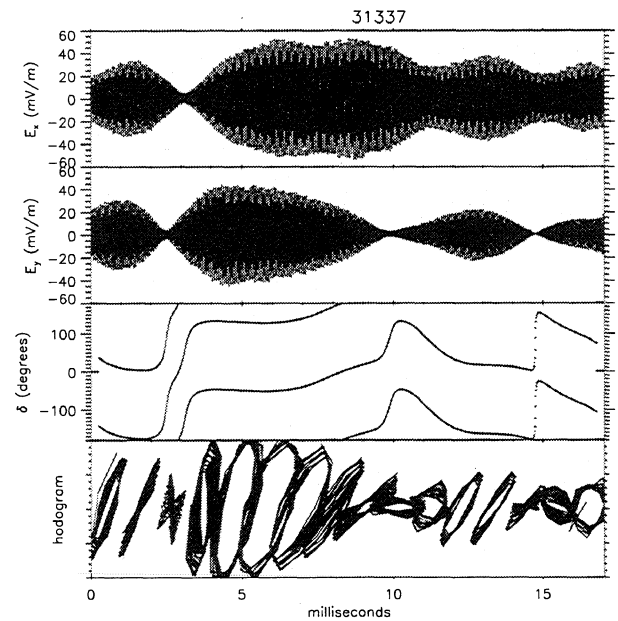

Figure 8. TDS waveform event at 0313:37 on April 20, 1996, an interval with a greater than 1-keV electron beam. The top two panels are the X and Y antenna measurements; the third panel shows the instantaneous phase shift between X and Y, and the bottom panel is a hodogram. As shown previously [*Bale et al.*, 1998], the wave electric field does not appear to be described by a simple longitudinal electrostatic wave. The rotating electric field could be due to mode conversion to z-mode, or tunneling in electron density fluctuations.

can be seen that the phase varies quickly; a purely longitudinal Langmuir wave would have phase 0 or π. The average phase can be shown to be a function of angle to the IMF [*Bale et al.*, 1998], and it was suggested that the observation is consistent with small wavenumber electomagnetic z-mode emission. Also the shape of the wavepacket is often quite different on the two antennas. *Kellogg et al.* [1999] have fitted the observations to two superposed waves, for both purely electrostatic and electromagnetic cases. They found that the fits to electromagnetic waves were generally better, though these fits do have more free parameters; they argue for both small-k z-mode waves and reflection, absorption, and scattering of electrostatic waves.

We have calculated the angle between the X antenna and the IMF direction by using 3-s (spin) resolution magnetic field data. Since the instrument chooses the largest-amplitude events on the X antenna preferentially for transmission to the ground, we can measure the angular occurrence of these events. Similar analyses have been published by *Anderson et al.* [1981], *Etcheto and Faucheux* [1984], and *Canu* [1990] using data from the ISEE spectral density instruments.

Figure 9 shows the peak and average amplitudes, as well as the probability density, against Ψ the angle between the spacecraft X antenna and the IMF direction. The top panel shows the peak amplitude for each of 1903 events, the middle panel is the average amplitude within 3° bins, with standard deviation error bars, and the bottom panel shows the probability density in 3° bins. It can be seen that while there is a strong angular selection effect, with peaks near 40° and 140°, the average amplitude does not vary much as a function of angle. The average magnetic latitude during these 1903 events was $\theta_B \approx 4.4°$, with a 23° standard of deviation; hence the probability density peaks at 40° and 140° are the result of a statistically nonzero Z component of the IMF. In Figure 10, we show the same parameters as a function of the angle Φ between the X antenna and the projection of the IMF into the X-Y GSE plane. Here the probability density (lower panel) peaks at 0° and 180°, while again the average electric field amplitude is relatively constant. We have calculated the probability density of angle for 273 events during which the IMF is within 3° of the X-Y plane (not shown) and find that this distribution approaches that of Figure 10. Hence the true distribution of peak electric field with respect to the IMF is very broadly peaked at 0° and 180°. Our probability density estimations (Figure 10) can be interpreted to be consistent with the results of previous studies [*Anderson et al.*, 1981; *Etcheto and Faucheux*, 1984; *Canu*, 1990; *Bale et al.*, 1998]; that is, the direction of the intense electric fields is centered on the IMF direction, but the angular distribution is very broad.

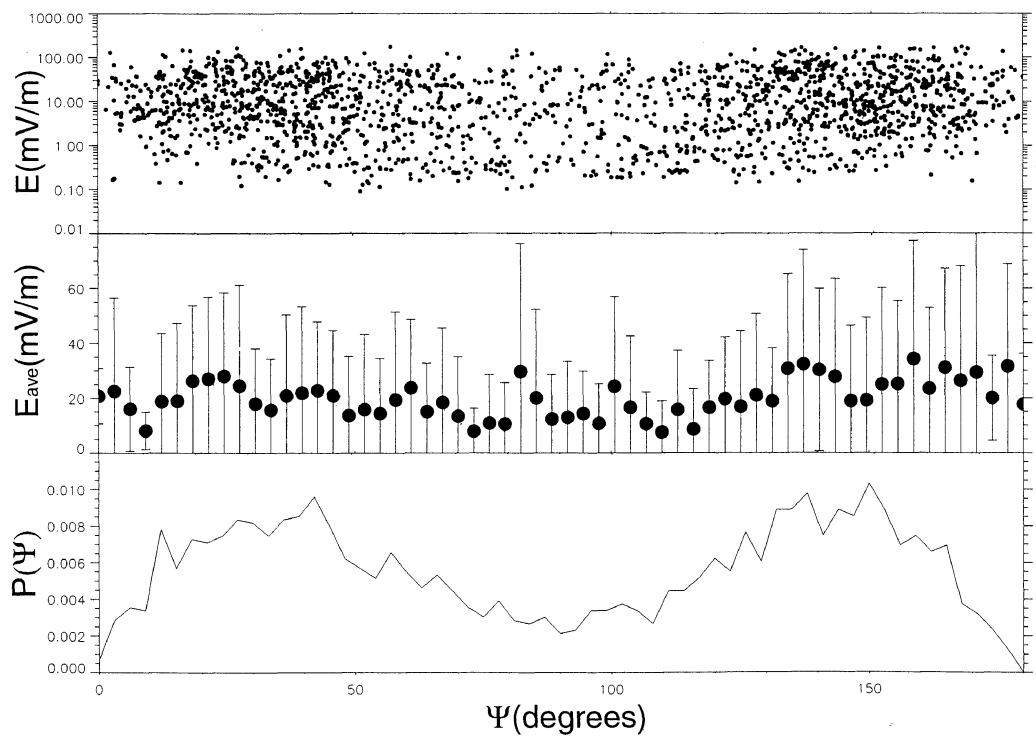

Figure 9. Antenna angle statistics. The angle Ψ between the spacecraft X antenna, which triggers the TDS waveform sampler, and the IMF is calculated for several hundred intense electron plasma waves. (top) Distribution of peak amplitudes against antenna angle, but no clear trend. (middle) Average (and standard deviation error bars) amplitude in 3° angular bins; again there is no apparent trend. (bottom) Probability distribution of angles. Since the TDS selects peak fields, in a 17-ms interval, this distribution reflects the occurrence of peak electric fields. The low counts at 0° and 180° are due to the fact that the IMF is rarely exactly in the ecliptic plane.

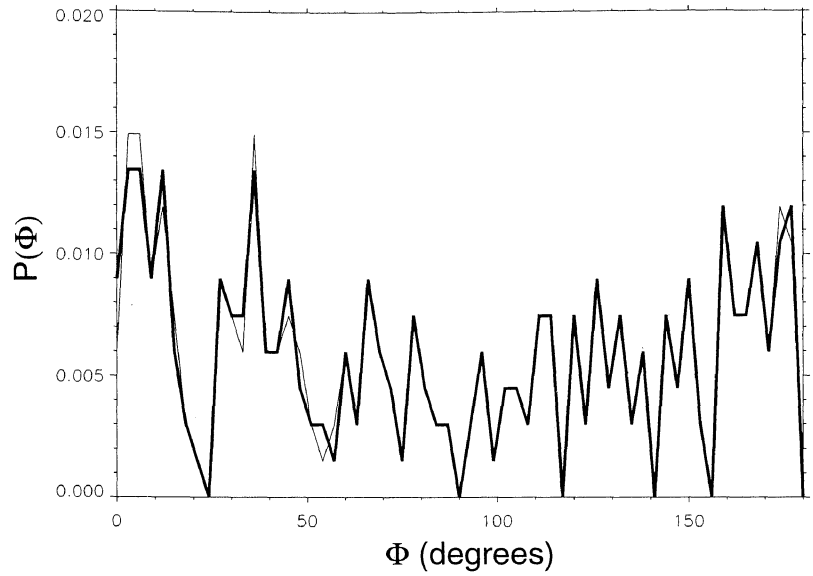

Figure 10. Probability distributions of antenna angle Ψ (thick line) and Φ, the angle between the X antenna and the projection of the IMF into the spacecraft spin plane (ecliptic) for a few hundred events in which the IMF lies within 3° of the IMF. The agreement of these distributions implies that the true distribution of peak amplitudes is peaked at 0° and 180°.

4. Discussion

In the above section, we described three characteristic observations of the intense plasma waves near the foreshock edge: (1) the electron beam that generates the waves is often energetic ($E_b \geq 1$ keV), (2) the bandwidth of the waves is smaller than would be expected of many well-developed nonlinear instabilities, and (3) the polarization of the waves in not field aligned and longitudinal. In this section, we discuss these results and consider a scenario of wave generation and evolution. A point that deserves discussion here is the position of the spacecraft relative to the electron foreshock edge. In principle, a calculation can be made to determine the depth of the spacecraft into the foreshock $DIFF \approx (v_{sw}/v_{beam})\ DIST$ given the distance along the tangent line ($DIST$) [e.g., *Filbert and Kellogg*, 1979], a shock model and the local IMF direction. For the observed >1-keV electrons, the expected depth would be $DIFF/DIST \approx (v_{sw}/v_{beam}) \leq 1/50$. On the other hand, calculations of the diffusion of the foreshock boundary due to magnetic turbulence in the IMF [*Zimbardo and Veltri*, 1996] show that the uncertainty in this calculation is of the order of $DIFF/DIST \approx 1/10$; hence the explicit calculation of foreshock depth is dominated by the pointing error of the local IMF due to turbulence.

4.1. Resonant Wavenumber, Index of Refraction, and Wave Scattering

In section 3, we saw that the electron distributions measured just at the solar wind-foreshock boundary often show enhanced flux above 1 keV, and possibly from above 4-5 keV. This implies that the electron beam that generates the source Langmuir waves is of the order of $v_b/v_{th} \geq$ 9-10, possibly as high as $v_b/v_{th} \approx 20$. The cutoff beam model of the foreshock edge [*Filbert and Kellogg*, 1979] allows for beam speeds at arbitrarily large velocities provided that there exists a sufficiently intense flux of suprathermal electrons. Observations of positive slope features in reduced (parallel) distribution functions [*Fitzenreiter et al.*, 1984; 1996] typically show beam features at $v_b/v_{th} \approx 5$, where the level of flux is quite high. However, these electron distribution functions are probably not sampled near the foreshock edge and therefore give lower beam speeds.

Assuming Landau coupling, the beam speed gives the resonant wavenumber $k_0 \approx \omega_{pe}/v_b$ of the instability and resonant refractive index $N_0 = k_0 c/\omega \approx c/v_b$. For beam speeds of $v_b/v_{th} \geq 10$, this gives $N_0 \leq 15$; the factor of 2 in beam speed is important in the following respect.

Figure 11 shows the dispersion relation for waves propagating near the electron plasma frequency in the solar wind. We assume $\omega_{pe}/\Omega_{ce} = 100$, $v_{th}/c = 1/150$, and a propagation angle $\theta = 8°$. The dispersion relation in Figure 11 is a superposition of the magnetized cold plasma modes [e.g., *Melrose*, 1984], with the warm plasma, magnetized Bohm-Gross dispersion $\omega^2 = \omega_{pe}^2 + 3k^2 v_{th}^2 + \Omega_{ce}^2 \sin^2\theta$, plotted as index of refraction $N = kc/\omega$ against ω/ω_{pe}. The dark band marked "resonance" shows the range of refractive index that corresponds to Landau coupling wavenumber $k_0 \approx \omega_{pe}/v_b$ for beam speeds of $v_b/v_{th} \approx$ 5-50. The dot-dash line above $N \approx 1$ corresponds to the Bohm-Gross dispersion which describes the propagation of purely longitudinal Langmuir waves. The continuation of the Bohm-Gross dispersion to small wavenumbers ($N << 1$) is the electromagnetic z-mode, which meets the o-mode (dashed line) near the "coupling point" $N \approx \Omega_{ce}/(\Omega_{ce} + \omega_{pe})$. The electromagnetic x-mode is the solid line with a

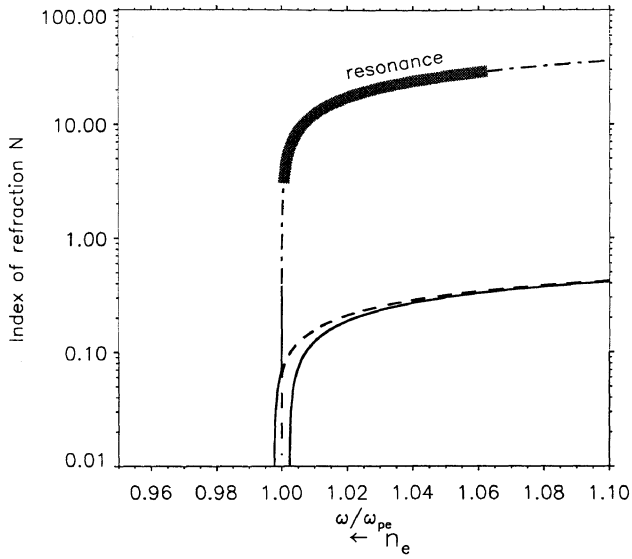

Figure 11. The dispersion relation of electron plasma waves, as index of refraction ($N = kc/\omega$) against ω/ω_{pe}. The dot-dash line is the warm plasma, magnetized Langmuir mode, which meets the electromagnetic z-mode at small N. Waves with beam speeds discussed in this paper have a resonant refractive index marked by the heavy bar. As they propagate into density enhancements, they must move leftward on the curve, and hence down to very small wavenumber.

cutoff above ω_{pe}. As was discussed previously in this context [*Muschietti et al.*, 1985;*Kellogg*, 1986; *Krauss-Varban*, 1989; *Bale et al.*, 1998; *Kellogg et al.*, 1999], the presence of small density fluctuations in the solar wind plasma represents a very strong scattering agent for electron plasma waves. This can be seen by studying Figure 11 and considering the propagation of plasma waves in the WKB approximation.

As a wave propagates into a density gradient with a scale size larger than the wavelength ($L >> \lambda$), the WKB approximation can be used to describe propagation. WKB states that the wave frequency and energy flux are conserved, while the wavenumber and amplitude vary to satify the dispersion relation locally. The WKB approximation and its validity are discussed in the appendix. A change in density $\delta n/n$ represents a change in the local plasma frequency $\delta\omega_{pe}/\omega_{pe} = 1/2\ \delta n/n$, and the Langmuir/$z$-mode dispersion changes wavenumber rapidly under such conditions. Waves generated with a resonant refractive index $N_0 \approx$ 3-30 (as discussed above) will be generated on the dark band marked resonance in Figure 11. Motion into a density enhancement will move the waves to the left on the dispersion curve, as ω_{pe} increases with ω held constant. Hence the waves must move down along he steep (nearly singular) portion of the curve to very small N (and hence k).

The observed large amplitude of the electric fields can, in part, be explained by the effect of wave scattering in the ambient solar wind density fluctuations. If waves are resonant near $N \approx 15$ and become scattered to smaller wavenumbers, say $N \approx 1$, then the wave amplitude will swell to $E/E_0 = \sqrt{N_0/N} \approx 3.9$. Hence a wave with an observed amplitude of $E \approx 75$ mV/m may have only grown to $E_0 \approx 20$ mV/m during resonance. On the other hand, waves encountering decreasing density will scatter to larger wavenumber, and hence smaller amplitude. However, owing to the shape of the dispersion relation (Figure 11) the effect is not nearly as strong. It should be noted that this effect may bias our observations; the TDS instrument selects the most intense events for input to the telemetry stream.

As waves scatter to smaller wavenumber, the number of electrons available for Landau damping also decreases significantly (and becomes zero at $N \leq 1$). At a given phase speed $v_\phi \approx \omega_{pe}/k$, waves will be Landau damped by electrons within a phase space region $(v_\phi - \Delta v, v_\phi + \Delta v)$, where Δv is from the bandwidth of the instability. If the waves scatter in the WKB approximation, then Δv may be considered constant. If we assume a power law suprathermal electron distribution $f \propto 1/v^\alpha$, then a little algebra shows that the number of electrons within $(v_\phi - \Delta v, v_\phi + \Delta v)$ scales as $n/n_0 \approx (N/N_0)^\alpha$, with the index of refraction. So for a power law index of 2 and $N = 2$ and $N_0 = 15$, we see that there are relatively few electrons $n/n_0 \approx 0.02$ available for Landau damping.

4.2. Electromagnetic Emissions

If beam resonant Langmuir waves are indeed scattered out to long wavelengths, this presents two options for the generation of electromagnetic emissions that differ from the paradigm.

At long wavelengths, Langmuir waves become mixed-polarization z-mode waves; near the coupling point $N \approx \Omega_{ce}/(\Omega_{ce} + \omega_{pe})$, the z-mode may tunnel through to the freely propagating o-mode branch for small angle of propagation. This effect is often invoked to explain fundamental plasma emission in other contexts (e.g., coronal, ionospheric, and auroral emissions). *Yin et al.* [1998c] have recently solved the one-dimenional differential equations that approximate this coupling. They find that ≈50% of the initial wave energy will couple to fundamental emission, while the other 50% is reflected back into the electrostatic Langmuir mode. This seems rather large; however, the conversion occurs at this level within a small regime of propagation angle so that the total efficiency is much smaller. One can easily calculate that this gives a brightness temperature of the order of $T_b \approx 10^{18}$ K (assuming a 45° half-angle cone of emission), while observed brightness temperatures are of the order of $T_b \approx 10^{15}$ K [e. g. *Burgess et al.*, 1987]. The reflection involved in this WKB violation may, however, produce the backward directed Langmuir waves necessary for short-wavelength coalescence to $2f_{pe}$.

Willes et al. [1996] have recently shown that the peak in the emission rate of the $L + L' \rightarrow T$ coalescence pro-

cess actually occurs at small wavenumber (long wavelength) $k_L \approx k_T/2$ for colinear waves; this corresponds to an index of refraction $N \approx \sqrt{3}/2$. If Langmuir waves are scattered to this low wavenumber, they will efficiently coalesce to produce $2f_{pe}$ emission. This process may occur within WKB and needs no backscattered electrostatic waves; however, it requires that WKB remain valid while the wave scatters to $N \approx \sqrt{3}/2$.

5. Summary

We have shown that the electron beam speed near the foreshock edge is often larger than previously assumed and that this has ramifications for the subsequent evolution of the beam-generated waves. Waves generated at smaller wavenumber are much more susceptible to strong scattering by the solar wind density fluctuations; this scattering takes the waves out of resonance with the beam and may move the wave energy into a regime where linear mode coupling to the electromagnetic *o*-mode becomes important, resulting in freely propagating emission at f_{pe}.

Appendix: WKB Approximation and Regime of Validity

The Wentzel-Kramers-Brillouin (WKB) approximation has been worked out for the case of Langmuir waves in solar wind density fluctuations [*Kellogg et al.*, 1999], however we let the wave packet envelope vary and get a slightly lower minimum wavenumber for the validity of WKB.

Assuming the one-dimensional propagation of a Langmuir wave into a density structure, the wave equation for oscillating electric field is

$$\frac{\partial^2 E}{\partial x^2} + k^2(x)E = 0. \tag{A1}$$

Seeking a solution of the form $E(x) = \varepsilon(x)\, e^{i\phi(x)}$, equation (A1) gives two equations (real part and imaginary part):

$$\frac{\partial^2 \varepsilon}{\partial x^2} + (k(x)^2 - (\frac{\partial \phi}{\partial x})^2) = 0 \tag{A2}$$

$$2\frac{\partial \phi}{\partial x}\frac{\partial \varepsilon}{\partial x} + \frac{\partial^2 \phi}{\partial x^2}\varepsilon = 0. \tag{A3}$$

If $\frac{\partial^2 \varepsilon}{\partial x^2}$ is considered small, then equation (A2) can be solved to give the standard WKB wavenumber solutions $\phi(x) = \pm \int dx\ k(x)$. Inserting this solution into equation (A3) gives the solution $\varepsilon(x) = \varepsilon_0 \sqrt{k_0/k(x)}$. Since for Langmuir waves the group speed is a linear function of k, $v_g = 3kv_{th}^2/\omega$, this is essentially the statement of conservation of energy flux $v_g\, E^2 = \text{const}$. From this relationship, it is easy to see that as the waves move into a region where the wavenumber is smaller (increasing density), the wave amplitude swells as $E \propto 1/\sqrt{k}$.

To find the regime of validity of WKB, we allow small changes in the wave phase $\partial\phi/\partial x = k(x)(1+\epsilon)$ in equation (A2) and use the relationship $\varepsilon(x) = \varepsilon_0 \sqrt{k_0/k(x)}$. This gives the condition

$$[\frac{3}{8}\frac{1}{k^4}(\frac{\partial k}{\partial x})^2 - \frac{1}{4}\frac{1}{k^3}\frac{\partial^2 k}{\partial x^2}] = \epsilon \ll 1, \tag{A4}$$

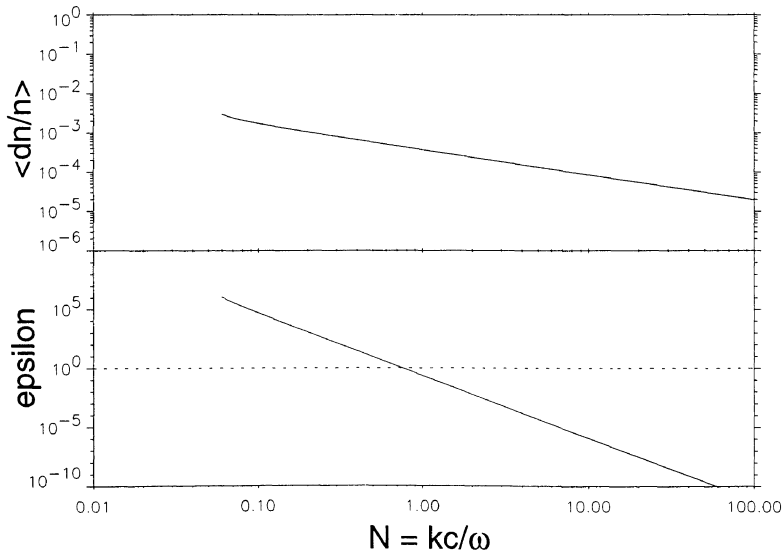

Figure A1. WKB approximation parameters. (top) Density fluctuation level at a scale given by the index of refraction, as integrated from power spectrum results of *Neugebauer* [1975]. (bottom) Smallness parameter ϵ, which describes the validity of one-dimensional WKB, $\epsilon << 1$. WKB would appear to be valid for $N > 1$.

where the second-derivative terms are again taken to be small. From the Bohm-Gross dispersion relation $\omega^2 = \omega_{pe}^2 + 3k^2 v_{th}^2$, we find that

$$|\frac{\partial k}{\partial x}| = \frac{\omega_{pe}^2}{3kv_{th}^2} \frac{1}{n} \frac{\partial n}{\partial x} \quad \text{(A5)}$$

using the definition of the plasma frequency $\omega_{pe} = \sqrt{4\pi ne^2/m}$. Then defining the index of refraction as $N \approx kc/\omega_{pe}$, the condition that $\epsilon \ll 1$ defines the regime of validity and

$$\epsilon \approx \frac{3}{288\pi^2} (\frac{c}{v_{th}})^4 (\frac{\delta n}{n})^2 \frac{1}{N^4} \ll 1, \quad \text{(A6)}$$

assuming that the relevant scale of fluctuations is comparable to the wavelength. We can evaluate this condition, using published power spectra of the solar wind density fluctuation spectrum.

There are few in situ observations of the solar wind electron density fluctuation spectrum in the short length-scale regime. *Celnikier et al.* [1983, 1987] estimated the density fluctuation spectrum by using the radio propagation experiment on the ISEE spacecraft. They found a breakpoint, above which the spectrum becomes flatter. *Unti et al* [1973] and *Neugebauer* [1975] measured the proton fluctuation spectrum using a Faraday cup on the OGO 5 spacecraft. Although there may be differences in the two spectra at small scales, we can use the result of *Neugebauer* [1975], who found a power law of relative density fluctuations $\delta n/n$. Extrapolating their inertial subrange, we have $P(f) \approx 5 \cdot 10^{-3} (f/f^*)^{-1.28}$ in units of Hz^{-1}, where f^* is the Doppler-shifted thermal ion gyroradius.

We integrate this power spectrum over one decade centered on each wavenumber to produce the top panel of Figure A1. The bottom panel shows the evaluation of ϵ from equation (A6) using the integrated density fluctuation spectrum and assuming $c/v_{th} = 150$. The dashed line is $\epsilon = 1$, and the curve crosses at $N \approx 0.5$.

So it seems that the WKB approximation may be a valid way to describe the evolution of the waves for index of refraction $N >> 0.5$. The curve is indeed very steep; at $N = 1$, the parameter ϵ is already ≈ 0.1, where the WKB may still be valid. Violation of the WKB approximation implies wave reflection and tunneling.

Acknowledgments. We thank the MFI team (principal investigator R. P. Lepping) at Goddard Space Flight Center for providing the spin resolution magnetic field data. Work at UC Berkeley is supported by NASA grants NAG5-2815 and NAG5-7961 to the University of California.

Michel Blanc thanks Gérard Chanteur and Iver Cairns for their assistance in evaluating this paper.

References

Anderson, K. A., R. P. Lin, F. Martel, C. S. Lin, G. K. Parks, and H. Reme, Thin sheets of energetic electrons upstream from the Earth's bow shock, *Geophys. Res. Lett., 6*, 401, 1979.

Anderson, R. R., G. K. Parks, T. E. Eastman, D. A. Gurnett, and L. A. Frank, Plasma waves associated with energetic particles streaming into the solar wind from the Earth's bow shock, *J. Geophys. Res., 86*, 4493, 1981.

Bale, S. D., D. Burgess, P. J. Kellogg, K. Goetz, and S. J. Monson, On the amplitude of intense Langmuir waves in the terrestrial electron foreshock, *J. Geophys. Res., 102*, 11,281, 1997.

Bale, S. D., P. J. Kellogg, K. Goetz, and S. J. Monson, Transverse z-mode waves in the terrestrial electron foreshock, *Geophys. Res. Lett., 25*, 9, 1998.

Bougeret, J.-L., et al., WAVES: The radio and plasma wave investigation on the Wind spacecraft, *Space Sci. Rev., 71*, 231, 1995.

Burgess, D., C. C. Harvey, J.-L. Steinberg, and C. Lacombe, Simultaneous observation of fundamental and second harmonic radio emission from the terrestrial foreshock, *Nature, 330*, 732, 1987.

Cairns, I. H., A theory for the Langmuir waves in the electron foreshock, *J. Geophys. Res., 92*, 2329, 1987.

Cairns, I. H., A semiquantitative theory for the $2f_{pe}$ radiation observed upstream from the Earth's bow shock, *J. Geophys. Res., 93*, 3958, 1988.

Cairns, I. H., and P. A. Robinson, First test of stochastic growth theory for Langmuir waves in Earth's foreshock, *Geophys. Res. Lett., 24*, 369, 1997.

Cairns, I. H., and P. A. Robinson, Strong evidence for stochastic growth of Langmuir-like waves in Earth's foreshock, *Phys. Rev. Lett., 82*, 3066, 1999.

Cairns, I. H., P. A. Robinson, and N. I. Smith, Arguments against modulational instabilities of Langmuir waves in Earth's foreshock, *J. Geophys. Res., 103*, 287, 1998.

Canu, P., Oblique broadband electron plasma waves above the plasma frequency in the electron foreshock: Linear theory and spacecraft observations, *J. Geophys. Res., 95*, 11,983, 1990.

Celnikier, L. M., C. C. Harvey, R. Jegou, M. Kemp, and P. Moricet, A determination of the electron density fluctuation spectrum in the solar wind, using the ISEE propagation experiment, *Astron. Astrophys., 126*, 293, 1983.

Celnikier, L. M., C. C. Harvey, R. Jegou, M. Kemp, and P. Moricet, Aspects of interplanetary turbulence, *Astron. Astrophys., 181*, 138, 1987.

Etcheto, J., and M. Faucheux, Detailed study of electron plasma waves upstream of the Earth's bow shock, *J. Geophys. Res., 89*, 6631, 1984.

Filbert, P. C., and P. J. Kellogg, Electrostatic noise at the plasma frequency beyond the Earth's bow shock, *J. Geophys. Res., 84*, 1369, 1979.

Fitzenreiter, R. J., A. J. Klimas, and J. D. Scudder, Detection of bump-on-tail reduced electron velocity distributions at the electron foreshock boundary, *Geophys. Res. Lett., 11*, 496, 1984.

Fitzenreiter, R. J., A. F. Vinas, A. J. Klimas, R. P. Lepping, M. L. Kaiser, and T. G. Onsager, Wind observations of the electron foreshock, *Geophys. Res. Lett., 23*, 1235, 1996.

Ginzburg, V. L., and V. V. Zheleznyakov, On the possible mechanisms of sporadic radio emission (radio emission in an isotropic plasma), *Sov. Astron.*, Engl. Transl., *2*, 653, 1959.

Goldman, M. V., D. L. Newman, J. G. Wang, and L. Muschietti, Langmuir turbulence in space plasmas, *Phys. Scr. T, 63*, 28, 1996.

Kellogg, P. J., Observations concerning the generation and propagation of type III solar bursts, *Astron. Astrophys., 169*, 329, 1986.

Kellogg, P. J., S. J. Monson, K. Goetz, R. L. Howard, J.-L. Bougeret, and M. L. Kaiser, Early Wind observations of bow shock and foreshock waves, *Geophys. Res. Lett., 23*, 1243, 1996.

Kellogg, P. J., K. Goetz, S. J. Monson, and S. D. Bale, Langmuir waves in a fluctuating solar wind, *J. Geophys. Res., 104*, 17,069, 1999.

Krauss-Varban, D., Beam instability of the z-mode in the solar wind, *J. Geophys. Res., 94*, 3527, 1989.

Lacombe, C., C. C. Harvey, S. Hoang, A. Mangeney, J.-L. Steinberg, and D. Burgess, ISEE observations of radiation at twice the solar wind plasma frequency, *Ann. Geophys., 16*, 113, 1988.

Lepping, R. P., et al., The WIND magnetic field investigation, *Space Sci. Rev., 71*, 207, 1995.

Lin, R. P., et al., A three-dimensional plasma and energetic particle investigation for the WIND spacecraft, *Space Sci. Rev., 71*, 125, 1995.

Melrose, D. B., *Instabilities in Space and Laboratory Plasmas*, Cambridge Univ. Press, New York, 1984.

Meyer-Vernet, N., and C. Perche, Tool kit for antennae and thermal noise near the plasma frequency, *J. Geophys. Res., 94*, 2405, 1989.

Muschietti, L., M. V. Goldman, and D. Newman, Quenching of the beam-plasma instability by large-scale density fluctuations in three dimensions, *Sol. Phys., 96*, 181, 1985.

Neugebauer, M., The enhancement of solar wind fluctuations at the proton thermal gyroradius, *J. Geophys. Res., 80*, 998, 1975.

Reiner, M. J., Y. Kasaba, M. L. Kaiser, H. Matsumoto, I. Nagano, and J.-L. Bougeret, Terrestrial $2f_p$ radio source location determined from WIND/Geotail triangulation, *Geophys. Res. Lett., 24*, 919, 1997.

Robinson, P. A., Clumpy Langmuir waves in type III radio sources, *Sol. Phys., 139*, 147, 1992.

Robinson, P. A., and I. H. Cairns, Stochastic growth theory of type III solar radio emission, *Astrophys. J., 418*, 506, 1993.

Scarf, F. L., R. W. Fredricks, I. M. Green, and M. Neugebauer, OGO 5 observations of quasi-trapped electromagnetic waves in the solar wind, *J. Geophys. Res., 75*, 3735, 1970.

Unti, T. W. J., M. Neugebauer, and B. E. Goldstein, Direct measurements of solar wind fluctuations between 0.0048 and 13.3 Hz, *Astrophys. J., 180*, 591, 1973.

Willes, A. J., P. A. Robinson, and D. B. Melrose, Second harmonic electromagnetic emission via Langmuir wave coalescence, *Phys. Plasmas, 3*, 149, 1996.

Yin, L., M. Ashour-Abdalla, M. El-Alaoui, J.-M. Bosqued, and J.-L. Bougeret, Plasma waves in the Earth's electron foreshock, 1, Time-of-flight electron distributions in a generalized Lorentzian plasma and dispersion solutions, *J. Geophys. Res., 103*, 29,595, 1998a.

Yin, L., M. Ashour-Abdalla, M. El-Alaoui, J.-M. Bosqued, and J.-L. Bougeret, Plasma waves in the Earth's electron foreshock, 2, Simulations using time-of-flight electron distributions in a generalized Lorentzian plasma, *J. Geophys. Res., 103*, 29,619, 1998b.

Yin, L., M. Ashour-Abdalla, M. El-Alaoui, J.-M. Bosqued, and J.-L. Bougeret, Generation of electromagnetic f_{pe} and $2f_{pe}$ waves in the Earth's electron foreshock via linear mode conversion, *Geophys. Res. Lett., 25*, 2609, 1998c.

Zimbardo, G., and P. Veltri, Spreading and intermittant structure of the upstream boundary of planetary magnetic foreshocks, *Geophys. Res. Lett., 23*, 793, 1996.

S. D. Bale, D. E. Larson, and R. P. Lin, Space Sciences Laboratory, University of California, Berkeley, CA 94720-7450. (bale@ssl.berkeley.edu; davin@ssl.berkeley.edu; rlin@ssl.berkeley.edu)

K. Goetz, P. J. Kellogg, and S. J. Monson, School of Physics and Astronomy, University of Minnesota, Minneapolis, MN 55455. (goetz@waves.space.umn.edu; kellogg@waves.space.umn.edu; monson@waves.space.umn.edu)

(Received November 8, 1999; revised February 23, 2000; accepted March 2, 2000.)